

# Plasma flow vs. magnetic feature-tracking speeds in the Sun

G. Guerrero<sup>1\*</sup>, M. Rheinhardt<sup>1</sup>, A. Brandenburg<sup>1,2</sup>, and M. Dikpati<sup>3</sup>

<sup>1</sup>*NORDITA, AlbaNova University Center, Roslagstullsbacken 23, SE-10691 Stockholm, Sweden*

<sup>2</sup>*Department of Astronomy, AlbaNova University Center, Stockholm University, SE-10691 Stockholm, Sweden*

<sup>3</sup>*High Altitude Observatory, National Center for Atmospheric Research †, 3080 Center Green, Boulder, Colorado 80301*

Accepted 1988 December 15. Received 1988 December 14; in original form 1988 October 11, Revision: 1.122

## ABSTRACT

We simulate the magnetic feature tracking (MFT) speed using advective-diffusive transport models in both one and two dimensions. By depositing magnetic bipolar regions at different latitudes at the Sun’s surface and following their evolution for a prescribed meridional circulation and magnetic diffusivity profiles, we derive the MFT speed as a function of latitude. We find that in a one dimensional surface-transport model the simulated MFT speed at the surface is always the same as the meridional flow-speed used as input to the model, but is different in a two-dimensional transport model in the meridional  $(r, \theta)$  plane. The difference depends on the value of the magnetic diffusivity and on the radial gradient of the latitudinal velocity. We have confirmed our results with two different codes in spherical and Cartesian coordinates.

**Key words:** magnetic fields – MHD – Sun: activity – convection

## 1 INTRODUCTION

At the solar surface magnetic features are observed in the form of active regions. Tracking the motion of such a structure individually, one finds in general a poleward migration which is suggestive of a poleward meridional flow at and just beneath the Sun’s surface. However, Doppler measurements of the poleward flow speed at the surface reveal a systematic difference from the speed inferred from magnetic feature-tracking (MFT): at low and mid latitudes, the latter is observed to be lower than the Doppler speed, but similar to it at high latitudes (see Fig. 10 of Ulrich 2010). Sunspots are usually discarded in such an analysis (Komm et al. 1993; Hathaway & Rightmire 2010) because their motion may be affected by their strong magnetic fields. To understand the physical origin of these differences, Dikpati et al. (2010) performed a simple test using a 2D (axisymmetric) advective-diffusive flux-transport model. They showed in simulations that, due to diffusive transport, the MFT speed can indeed be different from that of the meridional flow fed into the model. They attributed this difference to the latitudinal gradient of the radial component of the magnetic field, directed towards the equator at the equatorward side of an active region and towards the pole at its poleward side. They concluded that magnetic features drift poleward with a net speed that is lower than the flow speed at low latitudes and higher at high latitudes.

In non-axisymmetric two-dimensional  $(\theta, \phi)$  surface-transport models (e.g. Baumann et al. 2004; Sheeley 2010; Wang et al. 2009) one could likewise suppose that diffusion is the only agent that can prevent magnetic features from simply being advected with the meridional flow. However, differences between Doppler and MFT speeds have never been discussed for those models.

In this paper, we use both 1D and 2D advective-diffusive flux transport models to clarify to what extent the value of the magnetic diffusivity and its radial gradient influence the difference between the circulation and MFT speeds. Moreover, we will study the role of the radial gradient of the latitudinal flow velocity.

## 2 MODELS AND METHODS

For the sake of simplicity we consider the evolution of azimuthally averaged, purely poloidal, i.e., meridional fields. Quite generally, studying averaged fields requires the inclusion of an additional mean electromotive force  $\overline{\mathcal{E}}$  in the induction equation. Its major constituents are often described by the  $\alpha$  effect, turbulent pumping and turbulent diffusivity  $\eta_t$  (see, e.g., Moffatt 1978). However, only the latter will be taken into account here and assumed to be isotropic, yet possibly depending on depth. We do not claim that all other mean-field effects, in particular turbulent pumping, are negligible, but prefer to clarify the origin of the speed deviations in question by considering the effects in isolation. Thus, we focus here on the competition between diffusion and advection.

Our model is kinematic and we consider axisymmetric solutions of the induction equation in spherical coordinates  $(r, \theta, \phi)$

$$\frac{\partial \mathbf{B}}{\partial t} = \nabla \times (\mathbf{U} \times \mathbf{B} - \eta_T \nabla \times \mathbf{B}), \quad \nabla \cdot \mathbf{B} = 0, \quad (1)$$

with the total (molecular plus turbulent) magnetic diffusivity  $\eta_T = \eta + \eta_t$  and the *prescribed* velocity  $\mathbf{U}$ , i.e., we disregard the back-reaction of the magnetic field onto  $\mathbf{U}$ . The computational domain spans over a spherical half-shell  $R_b \leq r \leq R$ ,  $0 \leq \theta \leq \pi/2$  (i.e., from the pole to the equator), where  $R$  is the solar radius and the base of the convection zone is at  $R_b = 0.7R$ . The total diffusivity

\* E-mail: guerrero@nordita.org (GG)

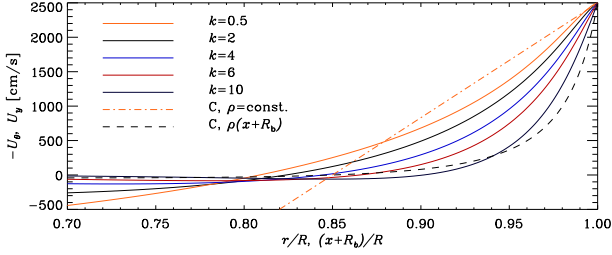


**Figure 1.** Solid lines: Radial profile of  $U_\theta(r, 57^\circ)$  for different  $k$  as indicated in the legend,  $n = 0.8$ , cf. Eq. (5). Broken lines: Cartesian velocity profile,  $U_y(x, L_y/2)$ , cf. Eq. (11).

$\eta_T$  is, unless specified otherwise, constant across the domain and considered a free parameter of the model.

For the 1D version of the model, we solve the radial part of Eq. (1) for  $B_r$  at  $r = R$ , as done in several surface-transport models (see, e.g., DeVore et al. 1984; Baumann et al. 2004):

$$\frac{\partial B_r}{\partial t} = -\frac{1}{R \sin \theta} \frac{\partial}{\partial \theta} \left[ \sin \theta \left( U_\theta B_r - \frac{\eta_T}{R} \frac{\partial B_r}{\partial \theta} \right) \right]. \quad (2)$$

Note that this equation is subject to the simplifying assumption  $B_\theta \ll B_r$  at the surface (see the Appendix of DeVore et al. 1984), the consequences of which will be assessed later when discussing our results. We solve Eq. (2) by using a second order finite difference scheme with 512 grid points<sup>1</sup>. The time integration is performed with an implicit (Crank-Nicholson) method.

For the 2D version we solve instead of Eq. (1) the corresponding equation for the  $\phi$  component of the vector potential  $\mathbf{A} = A \hat{e}_\phi$ , where  $\mathbf{B} = \nabla \times \mathbf{A}$ , and

$$\frac{\partial A}{\partial t} = -\frac{1}{s} (\mathbf{U} \cdot \nabla)(sA) + \eta_T \left( \nabla^2 - \frac{1}{s^2} \right) A, \quad s = r \sin \theta, \quad (3)$$

again utilizing finite differences (Lax-Wendroff scheme for first and centered second order scheme for second derivatives). For all simulations we use  $400^2$  grid points. A convergence analysis revealed that for the global evolution of the magnetic field a resolution of  $128^2$  grid points is already sufficient. However, a smoother profile of the estimated tracer velocity is obtained with the higher resolution. Time integration is done with the ADI method (for details see Guerrero & Muñoz 2004).

In modeling the meridional velocity  $\mathbf{U}$  we start with the corresponding mass flow  $\rho \mathbf{U}$  which is assumed steady and has thus to obey  $\nabla \cdot (\rho \mathbf{U}) = 0$  because of mass conservation. Hence it can be derived from a stream function  $\psi$  by  $\rho \mathbf{U} = \nabla \times (\psi \hat{e}_\phi)$ . Following Dikpati et al. (2010), we assume an adiabatic density profile

$$\rho(r) = \rho_0 (R/r - 0.97)^{1.5}, \quad (4)$$

where  $\rho_0$  is specified such that  $\rho(R) \approx 5 \cdot 10^{-3} \text{ g/cm}^3$ . For the stream function we choose the ansatz  $\psi = -\psi_0 F(r) \partial_\theta G(\theta)$  with

$$F(r) = \left( \frac{R}{r} - 0.97 \right)^n \left[ 1 - \left( \frac{r}{R} \right)^k \right] \left[ \left( \frac{R_b}{R} \right)^k - \left( \frac{r}{R} \right)^k \right], \quad (5)$$

$$G(\theta) = P_2(\cos \theta) + m P_4(\cos \theta), \quad (6)$$

where  $P_l$  is the Legendre polynomial of order  $l$ .  $F(r)$  guarantees vanishing  $U_r$  at the boundaries  $r = R_b, R$  assumed impenetrable.

<sup>1</sup> Same results are obtained for resolutions from 128 to 1024 grid points.

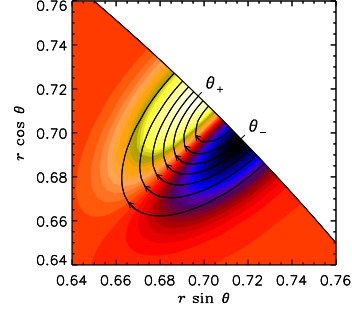


**Figure 2.** Bipolar region according to Eq. (7) for  $\theta_i = 45^\circ$ .  $\theta_\pm$  is the position of the centre of the polewards (positive) and equatorwards (negative) spot, respectively. Color coding:  $B_r$ .

The first factor in  $F(r)$ , resembling the density profile, is necessary to avoid local extrema of  $U_\theta$  within the domain which can be achieved by  $n = 0.8 \dots 1.2$ , depending on the value of  $k$ . Apart from that, the exponents  $n$  and  $k$  are free parameters of the model determining the value of the radial derivative of  $U_\theta$ . For fixed  $n$ , lower (higher) values of  $k$  result in a flatter (steeper) radial profile  $U_\theta(r)$  (see Fig. 1). Tuning the exponent  $n$  allows adjusting the  $U_\theta$  gradient just at the surface without changing it very strongly deeper down. So  $n$  can be employed for ensuring the stress-free boundary condition  $(\partial_r U_\theta)(R, \theta) = U_\theta(R, \theta)/R$ , usually imposed in, e.g., mean-field hydrodynamic models of stellar rotation and in direct numerical simulations of convection. Here, it can be expressed in the form  $h_r(R) = 1$ , where  $h_r(r)$  is the normalized radial gradient of  $U_\theta$ ,  $h_r(r) = r(d \ln F / dr)$ . For simplicity, we ignored this condition in most of our calculations and fixed  $n = 0.8$ . However, we have checked the influence of having the stress-free condition obeyed on our results in a number of cases with different values of  $n$ .

Further, the choice of  $m = -0.2$  results in a latitudinal surface profile  $U_\theta(R, \theta)$  which resembles Doppler velocity observations (see, e.g., Ulrich 2010), in particular the position of the surface maximum of  $U_\theta(R, \theta)$  is fairly well reproduced.  $\psi_0$  is adjusted such that this maximum is  $U_0 = 2500 \text{ cm/s}$ .

The initial magnetic field of a bipolar region is modelled as a flux loop in a meridional plane corresponding to two rings of concentrated magnetic flux on the surface of the sphere. We describe it by the vector potential

$$\mathbf{A} = A_0 \exp \left[ -\left( \frac{\theta - \theta_i}{w_\theta} \right)^2 \right] \exp \left[ -\left( \frac{r - R}{w_r} \right)^2 \right] \hat{e}_\phi, \quad (7)$$

where  $\theta_i$  is the initial latitudinal location of the center of the bipolar region. The initial separation between the positions at which  $B_r$  assumes its extrema at the surface, that is, the “spot separation” is  $\gtrsim \sqrt{2} w_\theta$ , whereas the depth to which the loop extends is controlled by  $w_r$ . We assume  $w_\theta = 0.02 (2.3^\circ)$  and  $w_r = 0.04R$  throughout this paper. For the corresponding field geometry see Fig. 2.

Magnetic boundary conditions are chosen to be consistent with a perfect conductor in  $r \leq R_b$  and to ensure continuity of  $\mathbf{B}$  with an external potential field at  $r = R$ . Comparisons with the simpler normal field condition  $\mathbf{r} \times \mathbf{B} = \mathbf{0}$  instead of the potential field condition showed no noticeable difference in the results. At the equator  $\mathbf{B}$  is assumed to be antisymmetric.

Both models were run over the model time interval  $T$ , being typically two weeks, for 20 equidistant initial latitudes  $\theta_i$  of the bipolar region between  $5^\circ$  and  $85^\circ$ . For measuring the latitudinal

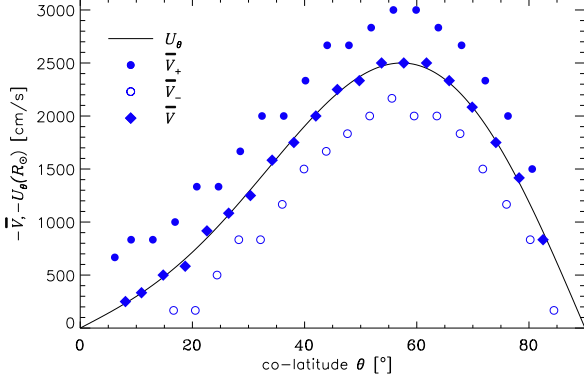


**Figure 3.** Tracking velocities for the 1D model (2) with  $\eta_T = 10^{12} \text{ cm}^2/\text{s}$ . Solid line: flow velocity  $U_\theta(R)$ , filled and open circles:  $\bar{V}_+$  and  $\bar{V}_-$ , respectively; diamonds: average  $\bar{V} = (\bar{V}_+ + \bar{V}_-)/2$ .

surface drift velocity of the flux loop, averaged over  $T$ , two different methods were employed. In the first one the position  $\theta_0$ , at which the normal magnetic field  $B_r$  vanishes, was followed. In the second, we trace the positions of the local maximum and minimum of  $B_r$  within the loop,  $\theta_+$  and  $\theta_-$ , respectively. The averaged latitudinal velocity was then defined as  $\bar{V}_0 = R(\theta_0(T) - \theta_0(0))/T$  in the first case and as the average of the two values  $\bar{V}_\pm = R(\theta_\pm(T) - \theta_\pm(0))/T$ , that is,

$$\bar{V} = (\bar{V}_+ + \bar{V}_-)/2 \quad (8)$$

in the second. We assign  $\bar{V}_0$  to the average colatitude  $(\theta_0(T) + \theta_0(0))/2$ , but  $\bar{V}$  to the average  $(\theta_+(T) + \theta_-(T) + \theta_+(0) + \theta_-(0))/4$ . As the profiles  $\bar{V}(\theta)$  and  $\bar{V}_0(\theta)$ , obtained directly in this way, turned out to be rather wiggly we fitted them just to  $U_\theta(R, \theta)$ , that is, to the function  $G$  in Eq. (6), but with an adjustable amplitude as fit parameter. For the highest diffusivity used and for starting latitudes  $\theta_i$  closest to the equator, the influence of this reflecting boundary becomes noticeable. This influence leads to an unrealistically low velocity of the equatorward (negative) spot which, in turn, corrupts  $\bar{V}$ . We use instead  $\bar{V}_0$  there.

### 3 RESULTS

#### 3.1 One-dimensional model

In simulations with high diffusivity,  $\eta_T = 10^{12} \text{ cm}^2/\text{s}$ , we find that the speed of the poleward spot,  $\bar{V}_+$ , is larger than the fluid velocity, whereas that of the equatorward spot,  $\bar{V}_-$ , is smaller; see Fig. 3. However, the average velocity  $\bar{V}$  matches the fluid velocity  $U_\theta$  fairly well. The velocity of the center of the bipolar region,  $\bar{V}_0$ , also coincides with it. For even higher values of  $\eta_T$ ,  $\bar{V}_+$  and  $\bar{V}_-$  deviate stronger from  $U_\theta$ , but the average continues to agree with it. For evolution times shorter than two weeks (e.g., one week or less) the curve for  $\bar{V}$  is more wiggly. However, it always follows the flow. These results agree with those of the 2D  $(\theta, \phi)$  model of Wang et al. (2009), where the poleward spots of the bipolar regions move faster than the fluid for a similar value of  $\eta_T$  (see their Fig.15).

#### 3.2 Two-dimensional model

Next, we study the evolution of a two-dimensional bipolar region by solving Eq. (3) using Eq. (7) as initial condition. As a represen-

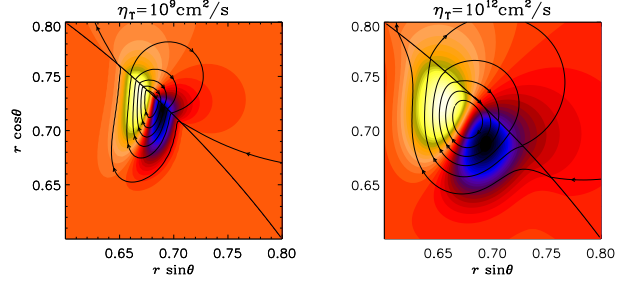


**Figure 4.** Magnetic field (solid lines) after two weeks of evolution of a bipolar region initially at  $\theta_i = 45^\circ$ , see Fig. 2. Color coding:  $B_r$ . Left:  $\eta_T = 10^9 \text{ cm}^2/\text{s}$ ; right:  $\eta_T = 10^{12} \text{ cm}^2/\text{s}$  (right).

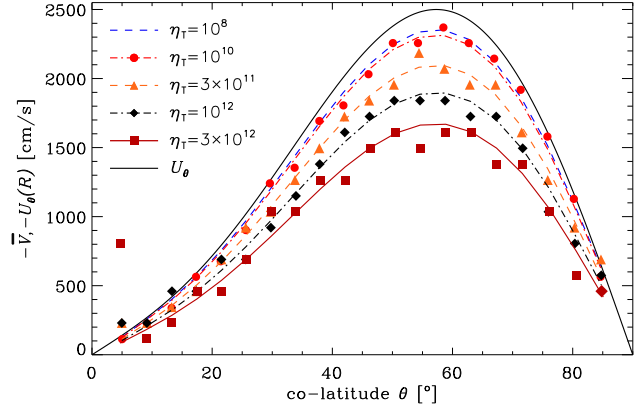


**Figure 5.** Tracking velocity  $\bar{V}(\theta)$  for  $10^8 \text{ cm}^2/\text{s} \leq \eta_T \leq 3 \times 10^{12} \text{ cm}^2/\text{s}$ ,  $k = 6$ . Solid/black: flow velocity  $U_\theta(R, \theta)$ . Symbols:  $\bar{V}$  according to Eq. (8), omitted for  $\eta_T = 10^8 \text{ cm}^2/\text{s}$  as mostly coinciding with those for  $\eta_T = 10^{10} \text{ cm}^2/\text{s}$ ; symbol for  $\eta_T = 3 \times 10^{12} \text{ cm}^2/\text{s}$ ,  $\theta = 85^\circ$  shows  $\bar{V}_0$ . Lines: data fitted to Eq. (6) with amplitude as fit parameter,  $m = -0.2$  fixed. Colors/symbols/line styles correspond to different values of  $\eta_T$  according to legend.

tative case, Fig. 4 shows the evolution for a bipolar region initially located at  $\theta_i = 45^\circ$ , using  $k = 6$  with either  $\eta_T = 10^9 \text{ cm}^2/\text{s}$  (left) or  $10^{12} \text{ cm}^2/\text{s}$  (right).

In contrast to the 1D model, where the profile  $\bar{V}(\theta)$  turns out to be independent of  $\eta_T$ , we find here a significant dependence. For small values of  $\eta_T$ , the “frozen-in” condition is fulfilled and thus the magnetic field lines appear indeed attached to the plasma flow. (The systematic offset between  $\bar{V}$  and  $U_\theta$  for  $\eta_T \rightarrow 0$ , visible in Figs. 5 and 6, is mainly due to the discretization errors.) For larger  $\eta_T$  ( $\gtrsim 3 \times 10^{11} \text{ cm}^2/\text{s}$ ), however, the diffusion time scale becomes similar to or even smaller than the advection time scale, and then there is an increasing departure from the “frozen-in” state. This becomes clear in Fig. 5, where  $\bar{V}(\theta)$  is shown for  $10^8 \leq \eta_T \leq 3 \times 10^{12} \text{ cm}^2/\text{s}$ . In general, the deviation from  $U_\theta$  increases everywhere with growing  $\eta_T$ , while for each  $\eta_T$  it adopts its largest value at intermediate latitudes of  $\approx 57^\circ$  where  $U_\theta$  peaks. Note that the simple fit based only on the amplitude, using the function  $G$  from Eq. (6), works remarkably well.

The top panel of Fig. 6 visualizes the dependence of  $\bar{V}$  on the radial variation of  $U_\theta$ , i. e., on the index  $k$  in Eq. (6). We present  $\bar{V}$  at the latitude where  $U_\theta$  peaks ( $\theta \approx 57^\circ$ ) as a function of  $\eta_T$  for  $k$  varying from 0.5 to 10. To minimize the effect of numerical

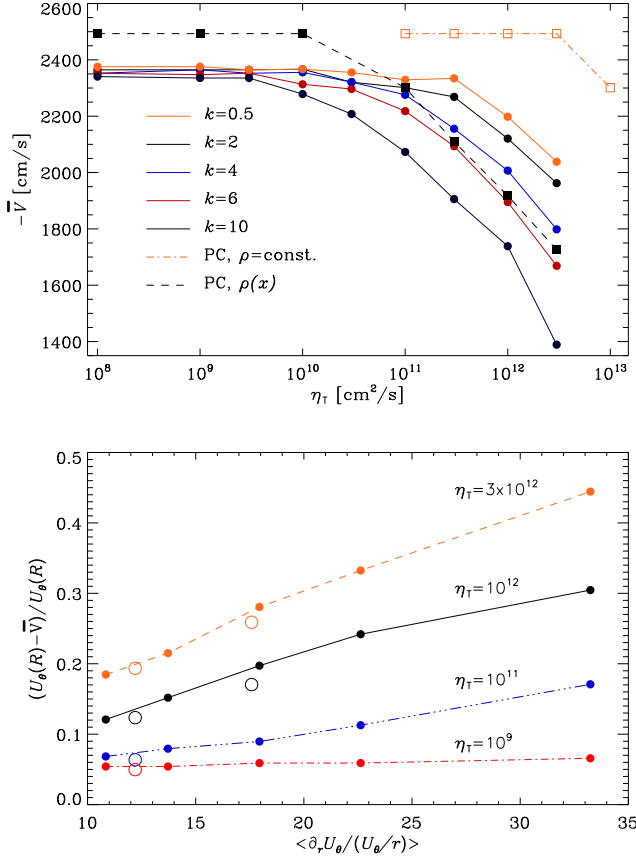


**Figure 6.** Upper panel: Maximum tracking velocity  $\bar{V}$  vs.  $\eta_T$  for different values of  $k$  in Eq. (6). Solid lines/filled circles correspond to the spherical model (values taken from fit curves). Broken lines/open squares correspond to the Cartesian model (C); dashed/filled squares: density according to Eq. (4), dash-dot/open squares: constant density. Lower panel, lines/closed circles: fractional speed difference,  $(U_\theta(R) - \bar{V})/U_\theta(R)$ , vs. the normalized radial gradient of  $U_\theta$ ,  $h_r(r)$ , averaged over  $r/R = 0.97 \dots 1$ . Open circles: stress-free boundary condition ensured in the profile (5) by  $(n, k) = (0.954, 4)$  for  $\langle h_r \rangle \approx 12$  and  $(1.194, 10)$  for  $\langle h_r \rangle \approx 17.5$ .

noise we have taken  $\bar{V}$  from fit curves. For  $k = 0.5$  (yellow line),  $\bar{V}$  does not depend on  $\eta_T$  up to  $10^{11}$  cm<sup>2</sup>/s. Beyond this value,  $\bar{V}$  starts to decrease. For increasing  $k$  the curves depart from the “frozen-in” domain at decreasing values of  $\eta_T$  being as small as  $\approx 3 \times 10^9$  cm<sup>2</sup>/s for  $k = 10$ . The bottom panel of the same figure shows the fractional velocity difference,  $(U_\theta(R) - \bar{V})/U_\theta(R)$ , as a function of the normalized radial gradient of  $U_\theta$ ,  $h_r(r)$ , averaged over the interval  $r = 0.97R \dots R$ , where the major part of the magnetic flux is residing. Note that for the highest diffusivity,  $3 \times 10^{12}$  cm<sup>2</sup>/s,  $\bar{V}$  is reduced by  $\approx 45\%$  at  $\langle h_r \rangle \approx 33$ . Employing our results for interpreting the data given in Fig. 10 of Ulrich (2010), we find that their speed reductions of about 30% do occur in our model, either for  $\eta_T = 3 \times 10^{12}$  cm<sup>2</sup>/s and  $\langle h_r \rangle \approx 20$  or for  $\eta_T = 10^{12}$  cm<sup>2</sup>/s and  $\langle h_r \rangle \approx 33$ . In the bottom panel of Fig. 6 some results are shown with the profile (5) adjusted to the stress-free boundary condition by fine-tuning of  $n$ . Obviously, there is only a slight reduction of the velocity difference in comparison with the unadjusted profile.

### 3.3 Dependency on $\eta_T(r)$

Having examined the influence of the radial profile of  $U_\theta$  on  $\bar{V}$ , one must ask whether also the radial profile of  $\eta_T$  has an effect. From an observational point of view this profile is unknown. Hence, the profiles so far considered in dynamo models are to some extent arbitrary. For instance, Dikpati & Gilman (2001) and Guerrero & de Gouveia Dal Pino (2007) have used a step function, with amplitudes of  $10^{10}$  cm<sup>2</sup>/s in the bulk of the convection zone and a value of  $\approx 10^{12}$  cm<sup>2</sup>/s for supergranular diffusion within the so-called near-surface shear layer. On the other hand, Pipin et al. (2011) considered a mixing length theory (MLT) estimation of  $\eta_t$ .

Here we consider both a step and an MLT profile defined by the following expressions (see the profiles in the top panel of Fig. 7):

$$\eta_T^{\text{step}} = \eta_{cz} + \frac{\eta_s - \eta_{cz}}{2} \left[ 1 + \text{erf} \left( \frac{r - 0.96R}{0.02R} \right) \right], \quad (9)$$

with  $\eta_s = 10^{12}$  cm<sup>2</sup>/s and  $\eta_{cz} = 10^{-2}\eta_s$ , and

$$\eta_T^{\text{MLT}} = \eta_{rz} + \frac{\eta_{cz} - \eta_{rz}}{2} \left[ 1 + \text{erf} \left( \frac{r - 0.71R}{0.02R} \right) \right] + \frac{\eta_s - \eta_{cz}}{2} \left[ 1 - \text{erf} \left( \frac{r - 0.93R}{0.04R} \right) \right], \quad (10)$$

where  $\eta_{rz} = 10^8$  cm<sup>2</sup>/s,  $\eta_s = 10^{13}$  cm<sup>2</sup>/s, and  $\eta_{cz} = 10^{-1}\eta_s$ .

We have performed numerical experiments with  $k = 6$  for  $U_\theta$  and a fixed surface value  $\eta_T(R) = 10^{12}$  cm<sup>2</sup>/s. The results, displayed in the bottom panel of Fig. 7, do not show marked differences between the three diffusivity profiles considered, and the MFT velocity profile is roughly the same. However, the separation between poleward and equatorward spots is smaller for the model with the step profile. The model with constant  $\eta_T$  exhibits an intermediate difference whereas in the model with the MLT profile the dispersion increases.

### 3.4 Comparison with Cartesian geometry

To assess the influence of the curvature in our spherical model we have repeated some of the simulations in a 2D ( $L_x \times L_y$ ) Cartesian box with aspect ratio  $(R - R_b) : R\pi/2$  and a simplified circulation velocity,

$$\mathbf{U} = \frac{1}{\rho} \nabla \times (\psi \hat{\mathbf{e}}_z), \quad \psi = \psi_0 \frac{x}{L_x} \left( \frac{x}{L_x} - 1 \right) \frac{y}{L_y} \left( \frac{y}{L_y} - 1 \right), \quad (11)$$

with  $(x, y)$  corresponding to  $(r, \theta)$ , respectively,  $\rho$  set either constant or to  $\rho(x + R_b)$  from Eq. (4), and  $\psi_0$  again adjusted to yield 2500 cm/s for the maximum surface velocity. Instead of the vacuum boundary condition at  $r = R$ , the simpler normal field condition  $\hat{\mathbf{e}}_x \times \mathbf{B} = \mathbf{0}$  was imposed there. These simulations were performed with the PENCIL CODE<sup>2</sup>, which uses sixth-order explicit finite differences in space and third order accurate time stepping method. For these runs we use 512<sup>2</sup> grid points.

The results, here with constant  $\eta_T$ , for both choices of  $\rho$ , are represented by broken lines in Fig. 6. The corresponding profiles  $U_y(x, L_y/2)$  are shown in Fig 1 with the same line styles. Clearly, these findings agree with those of the spherical model showing that the value of  $\eta_T$ , at which the frozen-in condition starts to fail, depends crucially on the radial ( $x$ ) gradient of  $U_y$  and varies here by about two orders of magnitude.

<sup>2</sup> <http://pencil-code.googlecode.com/>

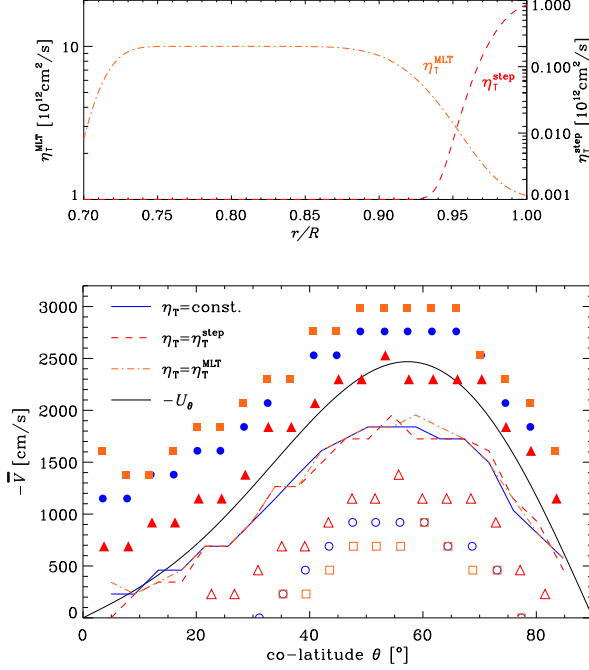


**Figure 7.** Top: Profiles of  $\eta_T$  used. Bottom: Corresponding tracking velocities  $\bar{V}$  for  $\eta_T(R) = 10^{12} \text{ cm}^2/\text{s}$ ,  $k = 6$ . Solid/black: flow velocity  $U_\theta(R)$ . Filled (open) symbols:  $\bar{V}_+$  ( $\bar{V}_-$ ).

#### 4 DISCUSSION AND CONCLUSIONS

Through 1D and 2D advective-diffusive models we have investigated the differences between the surface meridional flow speed obtained from Doppler measurements and that inferred from magnetic feature-tracking. In the one-dimensional simulations, the average velocity of the magnetic tracers always coincides with that of the flow, independently of the value of  $\eta_T$ . In 2D models, on the other hand, flow and feature-tracking velocities may diverge at higher diffusivities, for which the “frozen-in” condition does no longer hold. Further, the difference between these velocities depends on the radial gradient of the latitudinal velocity: the steeper  $U_\theta$ , the larger the difference. Using a different code we have verified that these results apply also in Cartesian geometry. To understand this dependence we refer to the induction equation (for simplicity in Cartesian coordinates), taken at the surface  $x = L_x$  (or  $r = R$ ) where  $U_x = \partial_y U_x = 0$ , so

$$\frac{\partial B_x}{\partial t} = -\frac{\partial}{\partial y}(U_y B_x) + \eta_T \left( \frac{\partial^2 B_x}{\partial x^2} + \frac{\partial^2 B_x}{\partial y^2} \right), \quad (12)$$

$$\frac{\partial B_y}{\partial t} = \frac{\partial}{\partial x}(U_y B_x - U_x B_y) + \eta_T \left( \frac{\partial^2 B_y}{\partial x^2} + \frac{\partial^2 B_y}{\partial y^2} \right). \quad (13)$$

Note that  $B_x$  is apparently decoupled from  $B_y$ , but at the price of being coupled to its second vertical derivative. In the case of small  $\eta_T$  (i.e., diffusion time larger than advection time), the evolution of  $B_x$  is governed by the first, advective, term in Eq. (12). In this case the magnetic field lines follow the fluid velocity locally (see curved magnetic field lines in the left hand panel of Fig. 4). In the case of larger  $\eta_T$  (diffusion time similar to or shorter than advection time), the diffusion term in Eq. (12) plays a significant role in the field evolution. The dependence on  $\partial_x^2 B_x$  can be eliminated by the solenoidal condition  $\partial_x B_x + \partial_y B_y = 0$ , by which the coupling between the two equations becomes obvious. Because  $B_y$  depends

explicitly on  $\partial_x U_y$ , the surface speed of  $B_x$  will clearly be modified by the fluid motion deeper down in the sub-surface layers. When ignoring  $B_y$  from the beginning, however, as done in DeVore et al. (1984), and many surface transport models afterwards, this influence will be lost. In spherical coordinates, the induction equation for  $B_r$  exhibits an analogous dependence on  $B_\theta$ , hence the same argument is valid.

Based upon our results for the difference between flow and feature-tracking speeds, one might think of inferring the thickness of the layer where the flow is poleward. This value, however, would depend on the surface diffusivity and on  $\partial_r U_\theta$ , both of which are poorly known. Hathaway (2011) has inferred an extreme flow pattern with a very shallow poleward flow ( $\approx 35 \text{ Mm}$  deep) which nevertheless can be brought into agreement with our findings, requiring a large radial gradient of  $U_\theta$ , that is,  $\langle h_r(r) \rangle \gtrsim 20$ , cf. Fig. 6. On the other hand, surface flux-transport models in two dimensions ( $\theta, \phi$ ) which disregard the radial derivatives in  $B_r$ , are probably overestimating the importance of advection in their results.

#### ACKNOWLEDGMENTS

This work started during the NORDITA program on predictability and data assimilation and is supported by the European Research Council under the AstroDyn research project 227952. MD thanks the support by NASA’s Living With a Star program through the grant NNX08AQ34G.

#### REFERENCES

- Baumann I., Schmitt D., Schüssler M., Solanki S. K., 2004, A&A, 426, 1075
- DeVore C. R., Sheeley Jr. N. R., Boris J. P., 1984, Sol. Physics, 92, 1
- Dikpati M., Gilman P. A., 2001, ApJ, 559, 428
- Dikpati M., Gilman P. A., Ulrich R. K., 2010, ApJ, 722, 774
- Guerrero G., de Gouveia Dal Pino E. M., 2007, A&A, 464, 341
- Guerrero G. A., Muñoz J. D., 2004, MNRAS, 350, 317
- Hathaway D. H., 2011, arXiv:1103.1561
- Hathaway D. H., Rightmire L., 2010, Science, 327, 1350
- Komm R. W., Howard R. F., Harvey J. W., 1993, Sol. Phys., 147, 207
- Moffatt H. K., 1978, Magnetic field generation in electrically conducting fluids. Cambridge Univ. Press, Cambridge
- Pipin V. V., Kuzanyan K. M., Zhang H., Kosovichev A. G., 2011, arXiv:1105.4285
- Sheeley Jr. N. R., 2010, in S. R. Cranmer, J. T. Hoeksema, & J. L. Kohl ed., SOHO-23: Understanding a Peculiar Solar Minimum Vol. 428 of Astronomical Society of the Pacific Conference Series, What’s So Peculiar about the Cycle 23/24 Solar Minimum? p. 3
- Ulrich R. K., 2010, ApJ, 725, 658
- Wang Y.-M., Robbrecht E., Sheeley N. R., 2009, ApJ, 707, 1372